

Further explorations of Skyrme-Hartree-Fock-Bogoliubov mass formulas. XVI. Inclusion of self-energy effects in pairing

S. Goriely,¹ N. Chamel,¹ and J. M. Pearson²¹*Institut d'Astronomie et d'Astrophysique, CP-226, Université Libre de Bruxelles, 1050 Brussels, Belgium*²*Département de Physique, Université de Montréal, Montréal (Québec), H3C 3J7 Canada*

(Received 20 January 2016; published 31 March 2016)

Extending our earlier work, a new family of three Hartree-Fock-Bogoliubov (HFB) mass models, labeled HFB-30, HFB-31, and HFB-32, is presented, along with their underlying interactions, BSk30, BSk31, and BSk32, respectively. The principle new feature is a purely phenomenological pairing term that depends on the density gradient. This enables us to have a bulk pairing term that is fitted to realistic nuclear-matter calculations in which for the first time the self-energy corrections are included, while the behavior of the nucleon effective masses in asymmetric homogeneous nuclear matter is significantly improved. Furthermore, in the particle-hole channel all the highly realistic constraints of our earlier work are retained. In particular, the unconventional Skyrme forces containing t_4 and t_5 terms are still constrained to fit realistic equations of state of neutron matter stiff enough to support the massive neutron stars PSR J1614–2230 and PSR J0348+0432. All unphysical long-wavelength spin and spin-isospin instabilities of nuclear matter, including the unphysical transition to a polarized state in neutron-star matter, are eliminated. Our three interactions are characterized by values of the symmetry coefficient J of 30, 31, and 32 MeV, respectively. The best fit to the database of 2353 nuclear masses is found for model HFB-31 ($J = 31$ MeV) with a model error of 0.561 MeV. This model also fits the charge-radius data with an root-mean-square error of 0.027 fm.

DOI: [10.1103/PhysRevC.93.034337](https://doi.org/10.1103/PhysRevC.93.034337)

I. INTRODUCTION

We have for some years been constructing semimicroscopic mass models based on the Hartree-Fock-Bogoliubov (HFB) method with Skyrme-type forces in the particle-hole channel and contact pairing forces in the particle-particle channel, together with phenomenological Wigner terms and correction terms for the spurious collective energy. While our model parameters are fitted to the mass data (and to some other measured quantities), our interest throughout this project has always been with the extrapolation out to the highly neutron-rich environments encountered in various astrophysical situations. Thus we were concerned in the first instance with predicting the masses of the experimentally inaccessible nuclei that are involved in the r -process of nucleosynthesis [1] and the outer crust of neutron stars (see, e.g., Refs. [2–5]).

An advantage of microscopic mass models over those based on the liquid-drop model is the fact that the underlying interactions can be used to calculate the equation of state (EOS) of both the inhomogeneous inner crust of neutron stars and the homogeneous core, effectively extrapolating the mass data to beyond the neutron drip line, and thereby making possible the sort of unified treatment of all regions of neutron stars that was presented in Ref. [6]. Given the applicability of our mass models to the elucidation of the r -process, both in supernova explosions and neutron-star mergers, it might be said that our models are relevant to a wide range of phenomena associated with the birth, life, and death of neutron stars.

Some of these phenomena are generally believed to be related to the existence of superfluids in the interior of neutron stars (for a recent review, see, e.g., Ref. [7]). In particular, the inner crust of a neutron star is thus expected to be permeated by a neutron superfluid. Although superfluidity in

pure neutron matter (NeuM) has been extensively studied, the properties of the neutron superfluid in the neutron-star crust still remain very uncertain due to the presence of neutron-proton clusters. Because of strongly attractive bare nucleon-nucleon interactions in the spin-singlet channel, both bound and unbound neutrons contribute to pairing and must therefore be treated consistently (see, e.g., Refs. [8–11]). For this reason, effective pairing forces that have been fitted only to pairing gaps in finite nuclei or only to pairing gaps in homogeneous nuclear matter are unlikely to yield reliable predictions in neutron-star crusts.

In this paper we are concerned with an improved treatment of the pairing channel of our models taking self-energy effects into account, but first we recall some general features of our earlier models. Up to and including model HFB-26 [12] our Skyrme force had the generalized 16-parameter form

$$\begin{aligned}
 v_{ij} = & t_0(1 + x_0 P_\sigma) \delta(\mathbf{r}_{ij}) \\
 & + \frac{1}{2} t_1(1 + x_1 P_\sigma) \frac{1}{\hbar^2} [p_{ij}^2 \delta(\mathbf{r}_{ij}) + \delta(\mathbf{r}_{ij}) p_{ij}^2] \\
 & + t_2(1 + x_2 P_\sigma) \frac{1}{\hbar^2} \mathbf{p}_{ij} \cdot \delta(\mathbf{r}_{ij}) \mathbf{p}_{ij} \\
 & + \frac{1}{6} t_3(1 + x_3 P_\sigma) n(\mathbf{r})^\alpha \delta(\mathbf{r}_{ij}) \\
 & + \frac{1}{2} t_4(1 + x_4 P_\sigma) \frac{1}{\hbar^2} [p_{ij}^2 n(\mathbf{r})^\beta \delta(\mathbf{r}_{ij}) + \delta(\mathbf{r}_{ij}) n(\mathbf{r})^\beta p_{ij}^2] \\
 & + t_5(1 + x_5 P_\sigma) \frac{1}{\hbar^2} \mathbf{p}_{ij} \cdot n(\mathbf{r})^\gamma \delta(\mathbf{r}_{ij}) \mathbf{p}_{ij} \\
 & + \frac{i}{\hbar^2} W_0(\boldsymbol{\sigma}_i + \boldsymbol{\sigma}_j) \cdot \mathbf{p}_{ij} \times \delta(\mathbf{r}_{ij}) \mathbf{p}_{ij}, \quad (1)
 \end{aligned}$$

where $\mathbf{r}_{ij} = \mathbf{r}_i - \mathbf{r}_j$, $\mathbf{r} = (\mathbf{r}_i + \mathbf{r}_j)/2$, $\mathbf{p}_{ij} = -i\hbar(\nabla_i - \nabla_j)/2$ (this is the relative momentum), P_σ is the two-body spin-exchange operator, and $n(\mathbf{r}) = n_n(\mathbf{r}) + n_p(\mathbf{r})$ is the total local density, $n_n(\mathbf{r})$ and $n_p(\mathbf{r})$ being the neutron and proton densities, respectively. The t_4 and t_5 terms are unconventional, being density-dependent generalizations of the t_1 and t_2 terms, respectively; they were introduced [13] in order to facilitate the fitting of a large amount of data, subject to several rather severe constraints. The full formalism for this generalization to the Skyrme force is presented in the Appendix of Ref. [13], but note that in all later papers we drop all the spin-current terms in J^2 and J_q^2 from the Hamiltonian density, where \mathbf{J}_q represents the nucleon spin-current densities ($q = n, p$ for neutron, proton respectively), and $\mathbf{J} = \mathbf{J}_n + \mathbf{J}_p$, as discussed in Refs. [14,15].

The parameters of this force, along with those associated with the pairing channel, the Wigner terms and the collective-energy correction, were fitted to all the 2353 measured masses of nuclei having N and $Z \geq 8$ given in the latest Atomic Mass Evaluation, AME 2012 [16] (or earlier versions). However, since all the astrophysical applications that we planned involve a long-range extrapolation from experimentally accessible environments to highly neutron-rich environments it is essential that our models incorporate as much well established theoretical knowledge of neutron-rich systems as possible. The most significant such constraint that we impose is to require that our mass fits be consistent, up to the densities prevailing in neutron-star cores, with the zero-temperature EOS of homogeneous pure NeuM, as calculated by many-body theory from realistic two- and three-nucleon forces. Several such EOSs have been published, but in Ref. [12] we settled on the one we refer to as LS2, corresponding to V18 in Ref. [17]. Almost as acceptable is the slightly softer one we label APR [18], but it led to slightly inferior mass fits. Although quantum Monte Carlo calculations [19] allow for EOSs that are still softer up to a density of about 0.5 fm^{-3} , such EOSs cannot support the heaviest observed neutron stars [20]. As discussed in Ref. [21], these astrophysical observations do not necessarily rule out a soft NeuM EOS since the core of a neutron star may consist of non-nucleonic matter. On the other hand, a NeuM EOS referred to as LS3 in Ref. [12], or to BOB in Ref. [17], while stiffer than LS2 at high densities, has to be rejected as too soft at low densities. This point was not made clear in Ref. [12], and we return to it below.

Requiring a high degree of stiffness for the high-density NeuM EOS comes at a considerable cost to the precision of the atomic mass fit, as shown in Ref. [22]. There we found that removing this constraint reduced the root-mean-square (rms) error from 0.549 MeV in the case of model HFB-24 to 0.512 MeV for a model having only a conventional 10-parameter Skyrme force (HFB-27*). Had we kept the same number of adjustable parameters the improvement in the fit on removing the NeuM constraint would have been still greater. Nevertheless, we regard the maintenance of this constraint as essential for the astrophysical applications that we have in mind. The ease with which such a constraint can be built into microscopic mass models represents another advantage over mass models based on the liquid-drop model.

In the mass fits of Ref. [12] we reduced the number of free parameters by imposing different fixed values of the nuclear-matter symmetry coefficient J . Of the five models thereby generated, characterized by various combinations of the two NeuM EOSs, LS2, and APR, and different values of J , the best overall fit was obtained for model HFB-24, for which $J = 30 \text{ MeV}$. Complete mass tables, running from one drip line to the other, were computed. The HFB-24 mass tables, along with the corresponding interactions (labeled BSk24, in accordance with our usual procedure), were used in the neutron-star calculations of Refs. [6,23,24], and also in a r -process calculation [25].

Our most recent mass model [26], HFB-29, is very similar to HFB-24, being based on the same 16-parameter form of Skyrme force, but an extra spin-orbit degree of freedom is introduced at the level of the energy-density functional, which becomes

$$\mathcal{E}_{so} = \frac{1}{2} W_0 \left[\mathbf{J} \cdot \nabla n + (1 + y_w) \sum_q \mathbf{J}_q \cdot \nabla n_q \right] \quad (2)$$

Setting $y_w = 0$ leads to the functional corresponding to the spin-orbit term in Eq. (1); other values of this parameter have no Skyrme equivalent, although $y_w = -1$ approximates closely the spin-orbit field given by relativistic mean-field theory. Fitting to the same mass data as for HFB-24, Ref. [26] led to an optimum value of 2.0 for y_w , with the rms error of the mass fit falling from 0.549 MeV for HFB-24 to 0.529 MeV.

II. THE PAIRING CHANNEL

In all our recent models published so far, including HFB-24 and HFB-29, we have attempted to impose on our pairing force realistic constraints comparable to those placed on the Skyrme force, our approach being essentially as described in Refs. [27–29]. That is, our pairing force, which acts only between like nucleons has the form

$$v^{\text{pair},q}(\mathbf{r}_i, \mathbf{r}_j) = f_q^\pm v^{\pi,q} [n_n(\mathbf{r}), n_p(\mathbf{r})] \delta(\mathbf{r}_{ij}), \quad (3)$$

where $v^{\pi,q} [n_n, n_p]$ is a functional of both the neutron and proton densities. The force is calculated analytically at each point in the nucleus (or, more generally, at each point in the inhomogeneous nuclear system) in question in such a way as to reproduce the 1S_0 pairing gaps of infinite nuclear matter (INM) of the appropriate density and charge asymmetry, as determined by many-body calculations with realistic two- and three-nucleon forces. This nuclear-matter constraint determines the strength of the pairing force almost completely, but we introduce some fine-tuning of the strengths in the form of the four global renormalization parameters f_q^\pm , which allow the overall strength to be slightly different for neutrons than for protons, and which also permit each of these strengths to depend on whether there is an even (f_q^+) or odd (f_q^-) number of nucleons of the charge type in question. In this way we take into account Coulomb effects as well as the slight violation of time-reversibility implicit in our use of the equal-filling approximation for odd nuclei.

The realistic pairing gaps $\Delta_q(n_n, n_p)$ to which we fit our pairing force are those given by the Brueckner calculations of

Cao *et al.* [30] in pure NeuM and in charge symmetric nuclear matter. The pairing gaps for arbitrary charge asymmetry were interpolated as in Ref. [27]. Solving the nuclear-matter BCS equations (to which the HFB equations reduce in a homogeneous system) then gives for the strength of our pairing force at the given densities (n_n, n_p) [28]

$$v^{\pi q}[n_n, n_p] = -\frac{8\pi^2}{I_q(n_n, n_p)} \left(\frac{\hbar^2}{2M_q^*(n_n, n_p)} \right)^{3/2} \quad (4)$$

with

$$I_q = \int_0^{\mu_q + \varepsilon_\Lambda} d\xi \frac{\sqrt{\xi}}{\sqrt{(\xi - \mu_q)^2 + \Delta_q^2}}, \quad (5)$$

where $M_q^*(n_n, n_p)$ is the nucleon effective mass and ε_Λ is the same cutoff as that used with $v^{\pi q}[n_n, n_p]$ in the finite-nucleus HFB calculations (note that the cut-off is taken above the chemical potential μ_q only, all states below being included). The chemical potential μ_q is approximated by

$$\mu_q = \frac{\hbar^2 k_{Fq}^2}{2M_q^*}, \quad (6)$$

where $k_{Fq} = (3\pi^2 n_q)^{1/3}$ is the Fermi wave number (see Section 3 of Ref. [28] for a discussion of this approximation). A further approximation that reduces significantly the computational load consists in using the analytic expression [31]

$$I_q = \sqrt{\mu_q} \left[2 \log \left(\frac{2\mu_q}{\Delta_q} \right) + \Lambda \left(\frac{\varepsilon_\Lambda}{\mu_q} \right) \right], \quad (7)$$

where

$$\Lambda(x) = \log(16x) + 2\sqrt{1+x} - 2\log(1 + \sqrt{1+x}) - 4. \quad (8)$$

Actually, Cao *et al.* [30] calculated gaps both with and without self-energy corrections. Now the excellent mass fits that we found in Ref. [27] and all our subsequent papers were obtained with the latter choice, the inclusion of self-energy corrections leading to gaps that are much smaller, too small to obtain a good mass fit (see Fig. 1). For internal consistency, we also set $M_q^*(n_n, n_p) = M$ in Eq. (4) in all our latest models. But gaps calculated with self-energy corrections are more realistic and thus more appropriate for the study of superfluidity in neutron stars. Thus in the present paper, with a view to extending the scope of our models to include the latter phenomenon, we modify our pairing functional (4) by fitting it to the gaps of Ref. [30] that were calculated with the inclusion of self-energy. Moreover, the effective mass $M_q^*(n_n, n_p)$ appearing in Eq. (4) is now taken as the one obtained from the Skyrme force. Then, in the attempt to simultaneously maintain the excellent mass fits that we have been obtaining, we add to the pairing force given by Eqs. (3) and (4) a phenomenological surface term, i.e., one dependent on the local density gradients. Thus in place of Eq. (3) we write

$$v^{\text{pair}, q}(\mathbf{r}_i, \mathbf{r}_j) = f_q^\pm \left[v^{\pi q}[n_n(\mathbf{r}), n_p(\mathbf{r})] + \kappa_q |\nabla n|^2 \right] \delta(\mathbf{r}_{ij}) \quad (9)$$

giving us thereby two extra parameters κ_p and κ_n .

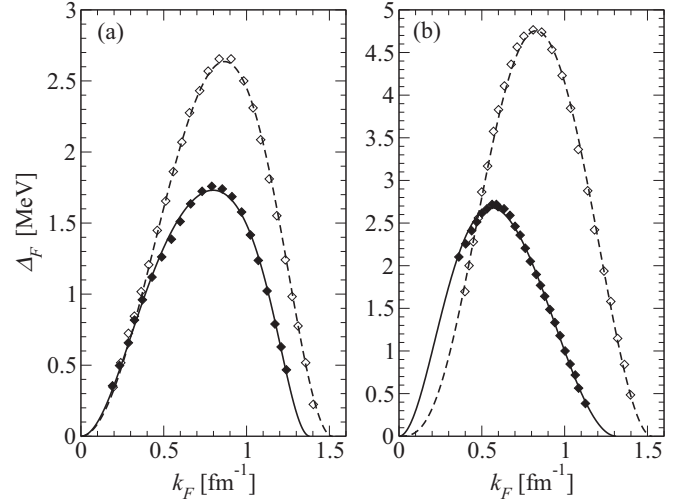


FIG. 1. 1S_0 pairing gaps in NeuM (a) and symmetric nuclear matter (b), as obtained by Cao *et al.* [30] with (filled symbols) and without (empty symbols) self-energy effects. In all cases, medium polarization effects are included. The curves represent our fits to their calculations.

III. CONSTRUCTION OF THE NEW MASS MODELS

Aside from the new form of pairing, the construction of the new models proceeds in much the same way as in the past: see in particular Sec. II of Ref. [12]. In particular both the form of the Wigner terms and that of the correction for the spurious collective energy are as in that paper. Thus the Wigner term to be added to the HFB energy calculated for the Skyrme and pairing forces is still written as

$$E_W = V_W \exp \left\{ -\lambda \left(\frac{N-Z}{A} \right)^2 \right\} + V'_W |N-Z| \exp \left\{ -\left(\frac{A}{A_0} \right)^2 \right\}, \quad (10)$$

while our estimate for the spurious collective energy again takes the form

$$E_{\text{coll}} = E_{\text{rot}}^{\text{crank}} \left[b \tanh(c|\beta_2|) + d|\beta_2| \exp \left\{ -l(|\beta_2| - \beta_2^0)^2 \right\} \right], \quad (11)$$

in which $E_{\text{rot}}^{\text{crank}}$ denotes the cranking-model value of the rotational correction and β_2 the quadrupole deformation, while all other parameters are determined as before. While the first term represents the rotational correction (see Ref. [12]), the second term takes account of the *deformation dependence* of the vibrational correction [since E_{coll} as given by Eq. (11) vanishes for spherical nuclei we must suppose that the vibrational correction for such nuclei is absorbed into the fitted force parameters].

Also as in Ref. [12], for nuclei with an odd number of nucleons we adopt the equal-filling approximation. Likewise, we drop the Coulomb exchange term for protons, a device that leads to a significant improvement in the mass fits, especially mirror-nucleus differences.

TABLE I. Parameters of the new interactions of this paper; for convenience we also show interaction BSk29 [26]. The first 17 lines show the Skyrme parameters, and the remaining lines the pairing parameters. Note that it is more convenient to show the x_2 parameter in the form $t_2 x_2$, the only way in which x_2 enters into the formalism.

	BSk30	BSk31	BSk32	BSk29
t_0 [MeV fm ³]	-2299.92	-2302.01	-2305.89	-3970.40
t_1 [MeV fm ³]	760.62	762.99	768.802	394.880
t_2 [MeV fm ³]	0	0	0	0
t_3 [MeV fm ^{3+3α}]	13782.7	13797.83	13828.2	22649.3
t_4 [MeV fm ^{5+3β}]	-500.000	-500.000	-500.000	-100.000
t_5 [MeV fm ^{5+3γ}]	-40.000	-40.000	-40.000	-150.000
x_0	0.821058	0.676655	0.528518	0.964850
x_1	2.675188	2.658109	2.608577	-0.0047741
$t_2 x_2$ [MeV fm ⁵]	-420.51	-422.29	-426.49	-1388.95
x_3	1.06250	0.83982	0.61796	1.14453
x_4	5.00	5.00	5.00	2.00
x_5	-12.00	-12.00	-12.00	-11.00
α	1/5	1/5	1/5	1/12
β	1/12	1/12	1/12	1/2
γ	1/4	1/4	1/4	1/12
W_0 [MeV fm ⁵]	62.466	62.174	63.700	64.600
y_w	2	2	2	2
f_n^+	1.00	1.00	1.00	1.00
f_n^-	1.07	1.06	1.06	1.05
f_p^+	1.00	1.00	1.00	1.01
f_p^-	1.06	1.04	1.06	1.07
κ_n [MeV fm ⁸]	-37425.8	-36630.4	-40184.7	0.0
κ_p [MeV fm ⁸]	-41876.7	-45207.2	-44933.1	0.0
ε_Δ [MeV]	6.5	6.5	6.5	16.0

In addition to the NeuM constraints already discussed in Secs. I and II, our fits to the 2353 experimental masses [16] are constrained to three discrete values of the symmetry coefficient J , namely 30, 31, and 32 MeV, generating thereby three different interactions, labeled BSk30, BSk31, and BSk32, respectively, along with the corresponding parameters of the Wigner terms and collective corrections; it will be seen that this range of values of J is sufficient to pick out an optimal value. Each of these three fits was also subjected to the following supplementary constraints:

- (i) An optimal fit to the charge-radii data [32].
- (ii) A value of $0.84M$ for the isoscalar effective mass M_s^* in charge-symmetric infinite nuclear matter (INM) at the appropriate equilibrium density n_0 . This value of M_s^* is the value indicated by the INM calculations of Ref. [30] used here to constrain the bulk component of the pairing, i.e., the first term of Eq. (9); it is slightly larger than the value of 0.8 used for our previous interactions.
- (iii) The density dependence of the neutron and proton effective masses at different asymmetries to conform to the realistic extended Brueckner-Hartree-Fock (EBHF) calculations of Refs. [30,33,34].
- (iv) An incompressibility K_v of charge-symmetric INM falling in the experimental range 240 ± 10 MeV [35].
- (v) The stability of NeuM and of β -equilibrated neutron-star matter (N*M), i.e., the homogeneous nucleon-lepton mixture of which neutron-star cores are

comprised, against an unphysical long-wavelength polarization at any density relevant to neutron-star cores [13,15].

- (vi) An EOS of charge-symmetric INM that is consistent with measurements in heavy-ion collisions of nuclear-matter flow over the density range $1.5\text{--}4.5n_0$ [36,37].
- (vii) A qualitatively acceptable distribution of potential energy among the four different spin-isospin channels in INM.

The resulting sets of interaction parameters (Skyrme and pairing), BSk30, BSk31, and BSk32, are given in Table I, the Wigner parameters in Table II, and those of the collective correction in Table III. For each interaction complete mass tables, labeled HFB-30, HFB-31, and HFB-32, respectively, have been constructed, running from one drip line to the other.

The quality of the mass fits, as measured by the deviations between the measured and calculated masses, is shown in

TABLE II. The Wigner parameters of the new models of this paper; for convenience we also show model BSk29 [26].

	HFB-30	HFB-31	HFB-32	HFB-29
V_w [MeV]	-1.90	-2.00	-2.20	-1.70
λ	300	450	300	440
V'_w [MeV]	0.70	0.70	0.60	0.94
A_0	30	32	35	26

TABLE III. Parameters of Eq.(11) for the collective correction.

	HFB-30	HFB-31	HFB-32	HFB-29
b (MeV)	0.74	0.73	0.73	0.80
c	10	10	10	10
d (MeV)	3.3	3.3	3.3	3.9
l	13	13	14	16
β_2^0	0.1	0.1	0.1	0.1

Table IV. The first line gives the model error σ_{mod} , as defined by Eqs. (42) and (43) of Ref. [38], for the complete data set of 2353 nuclei. The usual rms and mean (experimental-calculated) deviations are shown in the next two lines; the difference between lines 1 and 2 lies in the fact that σ_{mod} is defined to remove at least partially the experimental errors that contribute to the rms error, thereby giving a better estimate of the intrinsic error of the model. In any case, both the model and rms errors are minimal for model HFB-31, although the differences between HFB-30 and HFB-31 are arguably insignificant. Lines 4 and 5 give the rms and mean deviations for a subset consisting of the most neutron-rich measured nuclei, here taken as the 257 nuclei with neutron-separation energies $S_n \leq 5$ MeV. In this region of the nuclear chart, one of particular interest from the standpoint of our intended applications, the superiority of model HFB-31 is much more striking. The next two pairs of lines show the rms and mean deviations for the S_n and the β -decay energies Q_β of all measured nuclei; these differential

TABLE IV. The first line gives the model error [38] on all the 2353 measured masses [16]. The following four pairs of lines give the rms (σ) and mean ($\bar{\epsilon}$) deviations between experiment and predictions for the three models of this paper as well as for the HFB-29 model. The first pair of lines refers to all the 2353 measured masses M that were fitted [16], the second pair to the masses M_{nr} of the subset of 257 neutron-rich nuclei with $S_n \leq 5.0$ MeV, the third pair to the neutron separation energies S_n (2199 measured values), the fourth pair to β -decay energies Q_β (2065 measured values), the fifth pair to charge radii (884 measured values [32]), and the fifth pair to the model error on the 26 experimental neutron skin thicknesses from Ref. [47] or the 10 thicknesses with experimental error smaller than 0.04 fm. The last line gives the predicted ^{208}Pb charge radius.

	HFB-30	HFB-31	HFB-32	HFB-29
$\sigma_{\text{mod}}(M)$ [MeV]	0.564	0.561	0.576	0.521
$\sigma(M)$ [MeV]	0.573	0.571	0.586	0.529
$\bar{\epsilon}(M)$ [MeV]	0.003	-0.004	-0.007	-0.0252
$\sigma(M_{nr})$ [MeV]	0.683	0.659	0.700	0.671
$\bar{\epsilon}(M_{nr})$ [MeV]	0.038	-0.015	0.137	0.000
$\sigma(S_n)$ [MeV]	0.474	0.464	0.489	0.438
$\bar{\epsilon}(S_n)$ [MeV]	-0.008	0.000	-0.007	-0.008
$\sigma(Q_\beta)$ [MeV]	0.589	0.578	0.601	0.540
$\bar{\epsilon}(Q_\beta)$ [MeV]	0.009	0.006	-0.004	0.006
$\sigma(R_c)$ [fm]	0.026	0.027	0.027	0.026
$\bar{\epsilon}(R_c)$ [fm]	0.001	0.002	0.000	0.001
$\sigma_{\text{mod}}(26\theta)$ [fm]	0.009	0.005	0.012	0.013
$\sigma_{\text{mod}}(10\theta)$ [fm]	0.012	0.005	0.016	0.016
$\theta(^{208}\text{Pb})$ [fm]	0.133	0.151	0.170	0.134

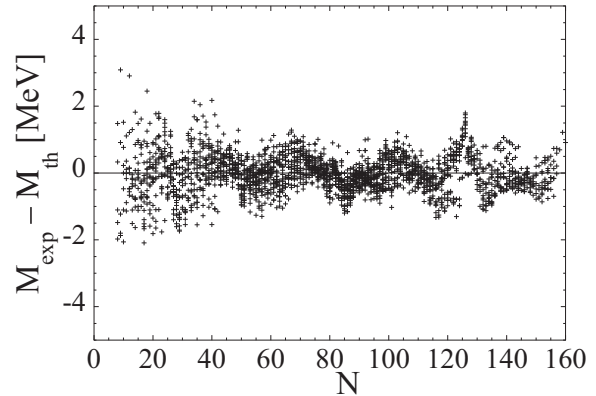


FIG. 2. Difference between measured [16] and HFB-31 masses as a function of the neutron number N .

quantities are of greater astrophysical relevance than the absolute masses, both for the r -process and the outer crust of neutron stars, and are also found to be better described by the HFB-31 model than the other two new ones. The last five lines in Table IV show that all models give essentially identical high-quality fits to the charge-radius data, but that neutron-skin thicknesses differ significantly and favor the HFB-31 model, despite the large uncertainties still affecting such experiments.

We illustrate in Fig. 2 the quality of the HFB-31 fit by plotting against N the difference $M_{\text{exp}} - M_{\text{calc}}$ for all the 2353 fitted nuclei. Qualitatively similar figures are obtained for HFB-30 and HFB-32.

Although the global rms deviation for the HFB-31 mass model is not quite as good as for each of the models from HFB-23 to HFB-29 [12,22,26], it is more realistic than any of these models in that it is the only one whose pairing takes account of self-energy and has a density-gradient term. Moreover, the measured neutron-rich nuclei are better fitted by HFB-31 than by any other of our models except HFB-27*, whose underlying pairing interaction is purely phenomenological, and the resulting EOS of N^*M is too soft to support the two massive pulsars PSR J1614-2230 and PSR J0348+0432. Therefore, this model is less appropriate for astrophysical applications.

We see from Table I that the strength parameter κ_q of our density-gradient pairing term is always negative, i.e., it is attractive. The presence of such a term can be understood physically as originating in the two nucleons in question tending to form a Cooper pairs through coupling with surface vibrations, just as Cooper pairs in a metallic superconductor are formed through coupling with lattice vibrations. Nevertheless, we stress that the form we have adopted for the gradient term in Eq. (9) is purely phenomenological, having been chosen for simplicity, there being just one parameter for neutron pairing, and one for proton pairing; also only the gradient of the total density is involved. Such a pairing force should be appropriate not only for the limiting case of finite nuclei and homogeneous nuclear matter, but also for the intermediate case of the inhomogeneous nuclear matter of the inner crust of neutron stars.

Our attractive density-gradient term is to be contrasted with the work of Ref. [39], which invoked a repulsive density-gradient term to account for various kinks in isotopic chains of measured charge radii. Not surprisingly, our models are

TABLE V. Parameters of infinite nuclear matter for the models of this paper.

	BSk30	BSk31	BSk32	BSk29
a_v [MeV]	-16.089	-16.110	-16.126	-16.049
n_0 [fm^{-3}]	0.1586	0.1586	0.1584	0.1578
J [MeV]	30.0	31.0	32.0	30.0
L [MeV]	41.5	53.1	65.5	45.2
K_{sym} [MeV]	-47.2	-15.8	19.3	-38.5
K_v [MeV]	243.8	244.0	244.1	245.5
K' [MeV]	302.4	303.0	303.6	274.5
M_s^*/M	0.84	0.84	0.84	0.80
M_v^*/M	0.73	0.73	0.74	0.73
G_0	0.42	0.37	0.33	0.62
G'_0	0.97	0.97	0.97	0.95
$n_c(\text{N}^*\text{M})$ [fm^{-3}]	0.99	1.01	1.03	0.99
$n_c(\text{NeuM})$ [fm^{-3}]	0.67	0.66	0.65	0.69

unable to reproduce the observed kinks, but if we had taken a positive value of κ_q in order to do so the mass fits would have deteriorated.

It should also be noted that the fit is found to be optimum for a pairing cut-off energy $\varepsilon_\Lambda = 6.5$ MeV above the Fermi energy, a value significantly lower than the usual 16 MeV obtained in all our previous forces. Such a low value of the cut-off also ensures a good fit of the pairing strength to the experimental $^1\text{S}_0$ nucleon-nucleon phase shifts in the dilute limit $n_q \rightarrow 0$ [40].

IV. PROPERTIES OF THE NEW MODELS

The most important parameters of INM are given in Table V; they are defined as in Ref. [14], except that we now denote by $n_c(\text{N}^*\text{M})$ and $n_c(\text{NeuM})$ the average baryon number densities above which causality is violated in N^*M and in pure NeuM, respectively. Let us recall that causality is violated if the speed of sound exceeds the speed of light.

It should be noted that the energy per nucleon a_v of symmetric INM at the equilibrium density, n_0 , is large in comparison to previously obtained values. This leads to a rather stiff mass parabola that could affect the extrapolation far away from stability, as discussed in Sect. IV H.

A. NeuM

As discussed in Sec. I, our new Skyrme forces were adjusted to reproduce realistic NeuM EOSs. As shown in Fig. 3, the resulting NeuM EOSs at subsaturation densities are compatible with the quantum Monte Carlo calculations of Ref. [19], as well as with the predictions of Ref. [41] based on chiral effective field theory. Moreover, increasing the symmetry coefficient significantly improves the EOS. This figure also shows that the EOS that we refer to as LS3 appears to be too soft in this density regime. At higher densities, Fig. 4 shows that the NeuM EOS obtained with our new forces are consistent with realistic calculations.

As can be seen from Table V, causality in pure NeuM is violated at densities above $\sim 0.65\text{--}0.67$ fm^{-3} due to the

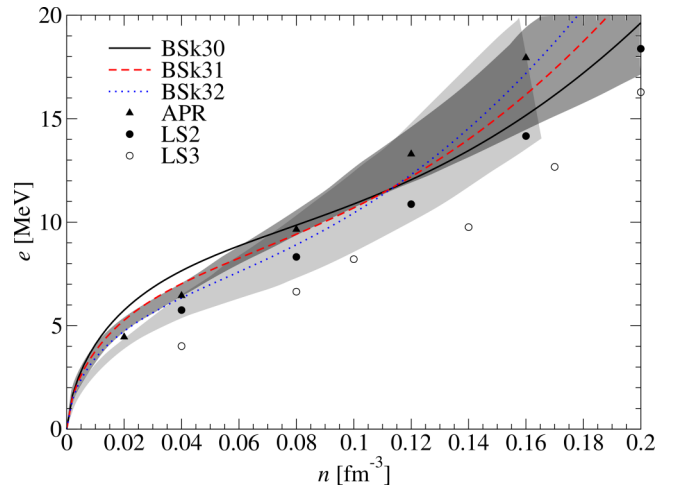


FIG. 3. Low-density zero-temperature EOS in NeuM for models BSk30 (solid line), BSk31 (dashed line), and BSk32 (dotted line). LS2 and LS3 correspond to the realistic EOSs referred to as V18 and BOB in Ref. [17], respectively. The shaded areas represent the constraints of Ref. [19] (dark) and of Ref. [41] (light).

neglect of relativistic effects at those densities in the underlying realistic EOSs of NeuM to which we have fitted our forces. However, the EOS of N^*M remains causal even in the most massive stars, as we discuss in Sec. IV E.

B. Symmetry energy

The parameters J and L shown in Table V for each of the models of this paper relate to the symmetry energy of INM: the former is the value of this energy at the saturation density n_0 , while the latter is defined by the density gradient of this energy at the same density (see Ref. [14]). While the mass models of this paper and of our Ref. [12] do not arrive at unique values of J and L , they do show the usual correlation between these two parameters, L increasing monotonically with J .

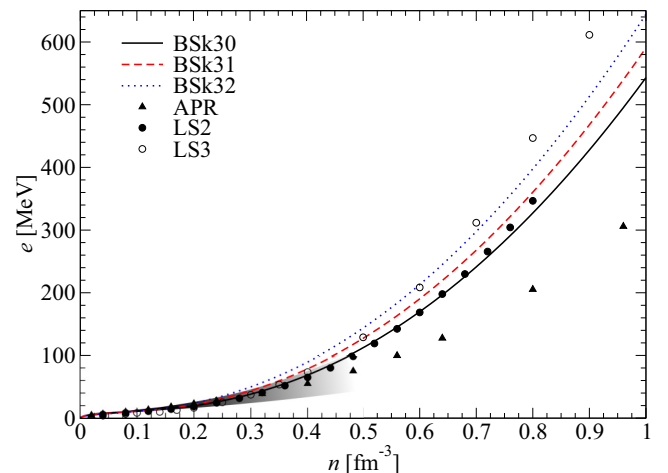


FIG. 4. Same as Fig. 3 for the high densities. The shaded area represents the constraints obtained in Ref. [19].

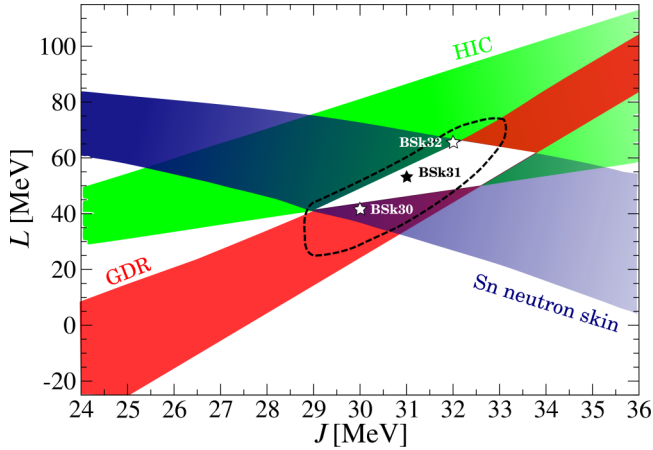


FIG. 5. Experimental constraints on the symmetry energy parameters (see text for details), taken from [43]. The stars indicate the values of J and L for BSk30, BSk31, and BSk32. The area within the dashed curve corresponds to the (L, J) values obtained in our previous fits.

Besides mass measurements several other types of experiment impose constraints on the values of J and L ; we summarize the analyses of Refs. [42,43] in Fig. 5. This figure shows the constraint deduced in Ref. [44] from heavy-ion collisions (HIC), the one derived in Ref. [45] from measurements of the neutron-skin thickness in tin isotopes, and the one obtained from the analysis of the giant dipole resonance (GDR) [43,46]. The zone of intersection of the corresponding three bands is denoted by the white lozenge-shaped figure, although it should be noted that the widths of the different bands displayed in Fig. 5 represent only the statistical error bars, and since the associated constraints are not directly derived from raw experimental data but rather are model dependent, it follows that the bands could be considerably wider than we have shown, making their zone of intersection larger. In any case, it will be seen that our best mass fit of this paper, BSk31, falls well within the permitted zone, while the other two lie close to it. Also, the best mass fit of Ref. [14], BSk24, lies within the permitted zone.

Concerning the predictions of our own models for neutron-skin thickness θ , we show in the last line of Table IV our values for the case of ^{208}Pb . For each given value of J our results are essentially the same as for Ref. [12]. However, when considering the antiproton scattering data [47] for the determination of neutron-skin thicknesses θ , we see in Table IV that for both the set of 26 values or the reduced set of ten values for which experimental errors are smaller than 0.04 fm the optimum predictions are found for HFB-31, i.e., $J = 31$ MeV. This result is in agreement with the comparison with nuclear masses which also favors $J = 31$ MeV in the present framework

Even though our objective is to provide interactions and mass models appropriate to astrophysical applications, rather than to determine the value of J , it is natural to ask how well our different mass fits determine J . The best mass fit of this paper, BSk31, has $J = 31$ MeV, while the best fit of our 2013 paper [12], BSk24, has $J = 30$ MeV. However, it has to be

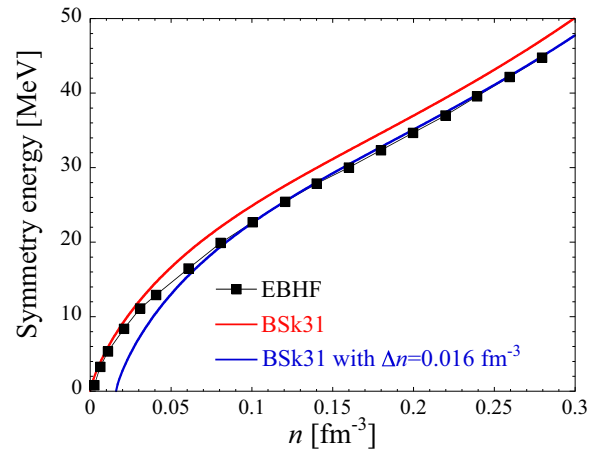


FIG. 6. Density dependence of the symmetry energy for BSk31. The EBHF calculation of [30] is shown for comparison. The blue curve is shifted by $\Delta n = 0.016 \text{ fm}^{-3}$ corresponding to the different saturation densities of the EBHF calculation and the one of BSk31.

noted that with its more realistic pairing and a two-parameter spin-orbit coupling, model BSk31 has a somewhat stronger physical basis than does model BSk24, and the quality of its mass fit is comparable to that of BSk24, if not unequivocally better. All in all, we regard interaction BSk31 to be the most reliable model we have generated for astrophysical purposes, but we refrain from expressing a preference for the value $J = 31$ MeV over 30 or even 32 MeV. Performing the sort of covariance analysis made by Mondal *et al.* [48] would hardly resolve the problem, since the error bars for all three models would almost certainly overlap strongly.

The density dependence of the symmetry energy is also in excellent agreement with the EBHF calculations of Ref. [30], as shown in Fig. 6. It should however be noted that the saturation of symmetric INM obtained by the EBHF calculations is found at a somewhat higher density, namely $n_0 = 0.175 \text{ fm}^{-3}$, a value that does not lead to an optimum description of nuclei, as shown by the poor nuclear mass prediction of the LNS Skyrme force fitted to reproduce the EBHF calculations in INM [30] (in particular, the LNS interaction underestimates the ^{208}Pb binding energy by some 80 MeV, see their Fig. 6 with $\Delta E/A \simeq -0.5$ MeV). We attempt to compensate this discrepancy by shifting the curve labeled BSk31 in Fig. 6 0.016 fm^{-3} to the right, this shift corresponding to the density difference in the saturation density between LNS and BSk31 force.

C. Effective masses

As shown in Table V, we impose on our interactions the realistic value of $M_s^* = 0.84M$ for the isoscalar effective mass at the saturation density n_0 of charge-symmetric INM, this being the value found by the EBHF calculations [30,33,34] at the density $n = 0.16 \text{ fm}^{-3}$, the approximate value of n_0 for all our interactions. On the other hand, the isovector effective mass, M_v^* , was left as a free parameter whose value emerged from the fits; the values shown in Table V are again calculated at the appropriate value of n_0 . Experimental estimates of

M_v^* vary widely: measurements of the isovector giant dipole resonance (IVGDR) in heavy nuclei, as summarized in Fig. 47 of Ref. [49], indicate that the value of M_v^*/M can range from 0.7 to 1 (this figure in effect plots M/M_v^*). However, the subsequent discussion in Ref. [49] points out that lower values are possible, which means that none of our models is in clear conflict with experiment. Moreover, all three models have, like all our previous models, $M_v^* < M_s^*$, which implies that the neutron effective mass M_n^* is larger than the proton effective mass M_p^* in neutron-rich matter, since the effective mass of a nucleon of charge type q in nuclear matter at density $n = n_n + n_p$ and asymmetry $\eta = (n_n - n_p)/n$ is given by

$$\frac{M}{M_q^*} = \frac{M}{M_s^*} \pm \eta \left[\frac{M}{M_s^*} - \frac{M}{M_v^*} \right], \quad (12)$$

where the upper (lower) sign is for neutrons (protons). This $M_n^* > M_p^*$ prediction is consistent with measurements of the IVGDR [50], and has been confirmed in many-body calculations with realistic forces [30]. With these latter calculations giving $M_s^* = 0.84M$ and $M_v^* = 0.73M$ at a density of $n_0 \simeq 0.16 \text{ fm}^{-3}$, we see that the magnitude of the splitting given by the new models is in excellent agreement with such realistic calculations.

Figure 7 shows for the three new models the density dependence of M_n^* and M_p^* , and compares them with the realistic EBHF predictions in asymmetric nuclear matter [30]. The three models show virtually the same density dependence of M_q^*/M . Note that the non-linearity of $1/M_s^*$ and $1/M_v^*$ with density is due to the terms in t_4 and t_5 . In particular, the non-monotonicity visible in Fig. 7 gives rise to a surface-peaked value of the neutron effective mass larger than 1, but only at very low densities, e.g., $n \lesssim 0.08 \text{ fm}^{-3}$ for an asymmetry $\eta = 0.4$.

D. Potential energy in the (S, T) channels

Fitting our forces to the mass data and the EOS of NeuM is not a sufficient condition for ensuring a realistic distribution of the potential energy per nucleon among the four two-body spin-isospin (S, T) channels in charge-symmetric INM. Figure 8 shows this distribution for each of our three new forces as a function of density, and compares with two different BHF calculations: ‘‘Catania 1’’, based on Ref. [17] and ‘‘Catania 2’’, based on Ref. [51]. Given the evident uncertainty in what the real distribution actually is, the level of agreement we have found with our new forces can be regarded as satisfactory. This would have been very difficult within the framework of conventional Skyrme forces and the term in t_5 has been indispensable in this respect (see the discussion in Ref. [50]). The importance of a realistic distribution of the potential energy among the (S, T) channels for deformation energy was discussed long ago in Refs. [52,53].

E. Maximum neutron-star masses

The neutron star PSR J1614–2230, and more recently PSR J0348+0432, have been shown to have a mass as high as $1.97 \pm 0.04 M_\odot$ for the former [54] and $2.01 \pm 0.04 M_\odot$ for the latter [55]. These neutron-star mass measurements give

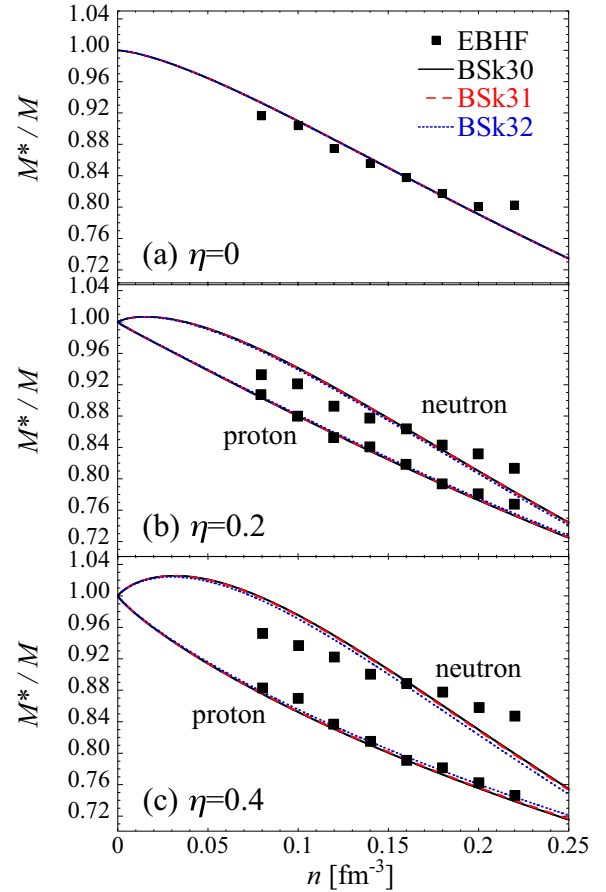


FIG. 7. Neutron and proton effective masses in symmetric nuclear matter (a) as well as in asymmetric matter with an asymmetry $\eta = 0.2$ (b) and 0.4 (c) obtained with the BSk30 (solid line), BSk31 (dashed line), and BSk32 (dotted line). The EBHF calculation of Ref. [30] is shown for comparison.

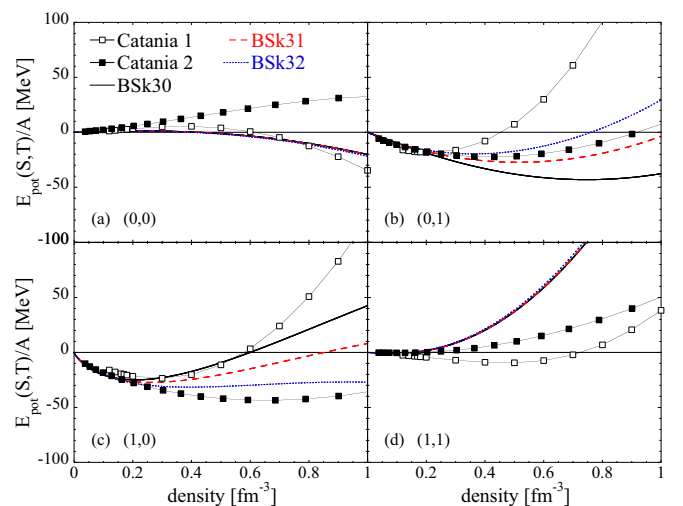


FIG. 8. Potential energy per particle E_{pot}/A in each (S, T) channel as a function of density for charge-symmetric INM. The open symbols correspond to the ‘‘Catania 1’’ BHF calculations [17], and the solid symbols to the ‘‘Catania 2’’ BHF calculations [51].

TABLE VI. Maximum neutron-star mass \mathcal{M}_{\max} and corresponding baryon number density n_{cen} at the center of the star for the different models.

Force	$\mathcal{M}_{\max}/\mathcal{M}_{\odot}$	n_{cen} [fm^{-3}]
BSk30	2.27	0.98
BSk31	2.26	0.97
BSk32	2.25	0.97

strong constraints on the EOS hence also on the effective interaction [20]. We calculated the maximum mass of nonrotating neutron stars for each of the new models of this paper solving the Tolman-Oppenheimer-Volkoff (TOV) equations [56,57]. We assume that neutron stars are homogeneous throughout, i.e., we neglect the inhomogeneities of the outer and inner crusts, and matter is supposed to be in β -equilibrium at zero temperature. We see from Table VI that all our new models are compatible with the existence of the massive neutron stars PSR J1614–2230 and PSR J0348+0432. Indeed, it turns out that the maximum mass is essentially the same for all models constrained by the same EOS of NuM, in particular, it seems to be relatively independent of the symmetry coefficient J . As can be seen from Tables V and VI, our models do not violate causality in any neutron stars.

F. Heavy-ion measurements of pressure

We have calculated the pressure in charge-symmetric INM as a function of density for our models with results that are essentially identical to those we obtained in Ref. [12]. That is, our models are consistent with measurements of nuclear-matter flow and kaon production in heavy-ion collisions [36,37], although close to the upper limit, as shown in Fig. 7 of Ref. [12].

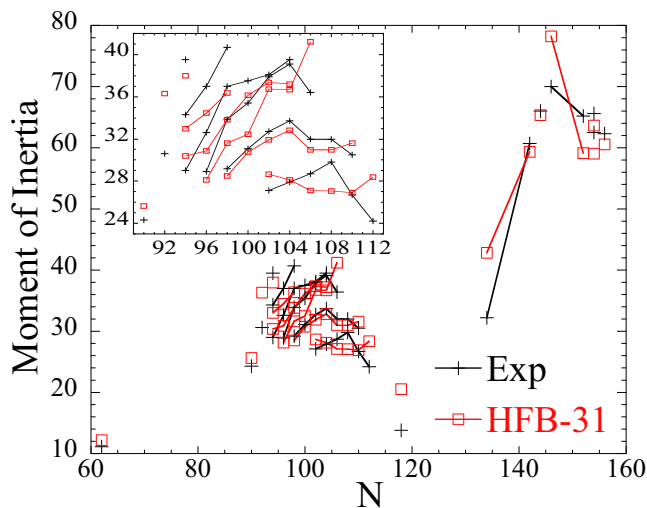


FIG. 9. Comparison between experimental (crosses) [58] and HFB-31 (squares) moments of inertia (expressed in units $\hbar^2 \text{MeV}^{-1}$). The insert is a zoom on the rare-earth isotopic chains for which data have been determined.

G. Moments of inertia

The moments of inertia of deformed even-even nuclei are known to be sensitive to the pairing description. With the first term of Eq. (11) representing the rotational correction, we can write the moment of inertia given by our HFB calculations as

$$\mathcal{I} = \frac{\mathcal{I}_{\text{crank}}}{b \tanh(c|\beta_2|)}, \quad (13)$$

where the parameters b and c of the rotational correction are given in Table III. We compare in Fig. 9 the HFB-31 predictions of the moment of inertia with the available data (HFB-30 and HFB-32 give rather similar estimates). We see that the calculated moments of inertia agree with experimental values within typically 10 to 15 %.

H. Mass extrapolations

Concerning the extrapolation of masses far away from experimental data, we show in Fig. 10, for all the nearly 6900 nuclei with $8 \leq Z \leq 110$ lying between the HFB-31 proton and neutron drip lines, the deviations between our two best-fit mass models, i.e., HFB-30 and HFB-31, as well as between the two mass models with the largest difference in the symmetry coefficient, i.e., HFB-30 with $J = 30 \text{ MeV}$ and HFB-32 with $J = 32 \text{ MeV}$. While in the first case, deviations are restricted

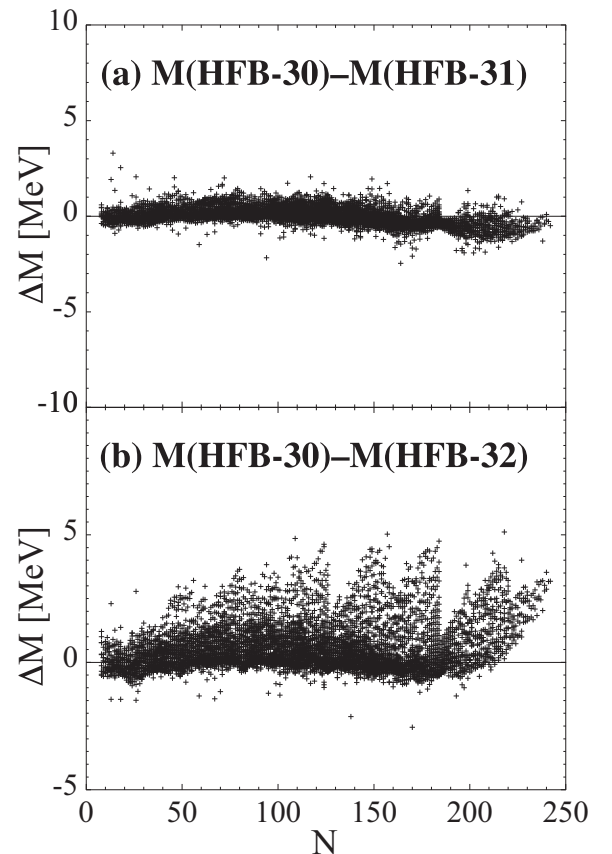


FIG. 10. (a) Differences between HFB-30 and HFB-31 mass predictions for all 6884 nuclei included in the tables. (b) Differences between HFB-30 and HFB-32 mass predictions

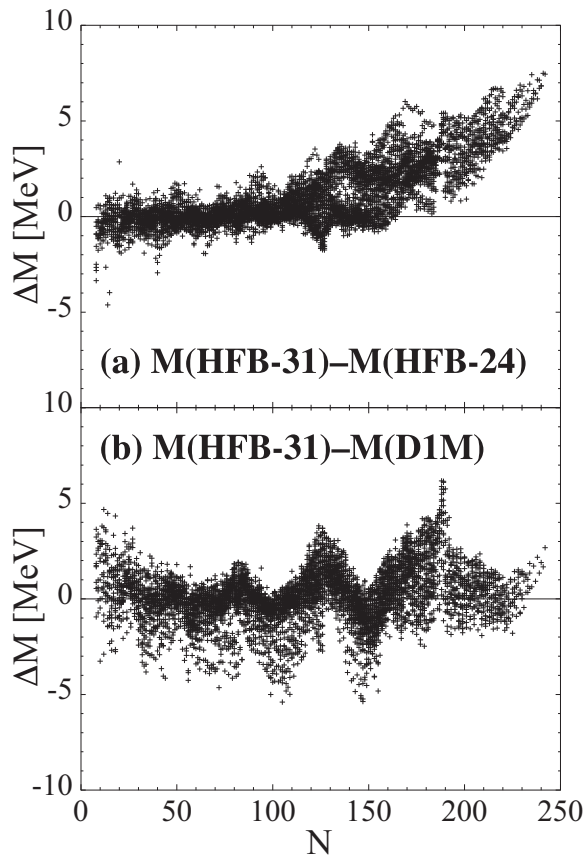


FIG. 11. (a) Differences between HFB-31 and HFB-24 [12] mass predictions for all 6884 nuclei included in the tables. (b) Differences between HFB-31 and D1M [59] mass predictions

to the narrow range of ± 2 MeV, much larger discrepancies, up to 5 MeV, are found between HFB-30 and HFB-32 when approaching the neutron drip line. In addition, it is noteworthy that the lower the J value the larger the masses predicted when approaching the neutron drip line, as already found and discussed in Ref. [12].

In Fig. 11, we compare the HFB-31 predictions with those of our mass model HFB-24 and the Gogny-HFB mass calculation based on the D1M force [59]. We see that the differences are relatively small except for the heaviest nuclei

($Z > 80$) and as the neutron-drip line is approached ($N > 160$). However, it is noteworthy that in the comparison with HFB-24 it is the *higher* J value that is associated with the larger masses. Conceivably the different treatment of the pairing and the different spin-orbit terms are playing a dominant role here. Non-negligible deviations are found with respect to the D1M mass model, especially in the vicinity of the $N = 126$ or 184 neutron shell closures.

V. CONCLUSION

This paper describes the latest effort in our long-running project of developing HFB mass models that give precision fits to all the available mass data while at the same time respecting the constraints appropriate to the treatment of highly neutron-rich environments of astrophysical interest. The present paper extends our previous work by including a phenomenological pairing term that depends on the density gradient. In this way it is possible for the first time to have a bulk pairing term that is fitted exactly to the realistic nuclear-matter calculations of Ref. [30] with self-energy corrections. At the same time, nucleon effective masses as predicted by our new Skyrme forces are found to be in excellent agreement with realistic calculations in asymmetric homogeneous nuclear matter. A two-parameter spin-orbit term, as introduced in Ref. [26], is also used. Our preferred model, HFB-31, fits 2353 measured masses with a model error of 0.561 MeV, and gives a precision fit to measured charge radii. Its underlying interaction, BSk31, has a symmetry coefficient J of 31 MeV and a slope $L = 53.1$ MeV, that are compatible with current laboratory constraints. The fit to realistic NeuM EOS and the empirical constraints from heavy-ion collision experiments ensure a reliable extrapolation of our models to the high densities found in neutron stars. As a matter of fact, all our models are consistent with the existence of the massive neutron stars PSR J1614–2230 and PSR J0348+0432. For all these reasons, we believe that our new models are particularly well suited for the description of neutron star interiors, and especially of neutron superfluidity in their inner crust.

ACKNOWLEDGMENT

S.G. and N.C. acknowledge financial support from FNRS (Belgium), J.M.P. that of NSERC (Canada).

[1] M. Arnould, S. Goriely, and K. Takahashi, *Phys. Rep.* **450**, 97 (2007).
 [2] X. Roca-Maza and J. Piekarewicz, *Phys. Rev. C* **78**, 025807 (2008).
 [3] J. M. Pearson, S. Goriely, and N. Chamel, *Phys. Rev. C* **83**, 065810 (2011).
 [4] N. Chamel, R. L. Pavlov, L. M. Mihailov *et al.*, *Phys. Rev. C* **86**, 055804 (2012).
 [5] S. Kreim, M. Hempel, D. Lunney, and J. Schaffner-Bielich, *Int. J. Mass Spectrom.* **349-350**, 63 (2013).

[6] J. M. Pearson, N. Chamel, A. F. Fantina, and S. Goriely, *Eur. Phys. J. A* **50**, 43 (2014).
 [7] D. Page, J. M. Lattimer, M. Prakash, and A. W. Steiner, in *Novel Superfluids*, Vol. 2, edited by Karl-Heinz Bennemann and John B. Ketterson (Oxford University Press, Oxford, 2014), p. 505.
 [8] M. Baldo, E. E. Saperstein, and S. V. Tolokonnikov, *Eur. Phys. J. A* **32**, 97 (2007).
 [9] N. Chamel, S. Goriely, J. M. Pearson, and M. Onsi, *Phys. Rev. C* **81**, 045804 (2010).

- [10] F. Grill, J. Margueron, and N. Sandulescu, *Phys. Rev. C* **84**, 065801 (2011).
- [11] A. Pastore, *Phys. Rev. C* **91**, 015809 (2015).
- [12] S. Goriely, N. Chamel, and J. M. Pearson, *Phys. Rev. C* **88**, 024308 (2013).
- [13] N. Chamel, S. Goriely, and J. M. Pearson, *Phys. Rev. C* **80**, 065804 (2009).
- [14] S. Goriely, N. Chamel, and J. M. Pearson, *Phys. Rev. C* **82**, 035804 (2010).
- [15] N. Chamel and S. Goriely, *Phys. Rev. C* **82**, 045804 (2010).
- [16] G. Audi, M. Wang, A. H. Wapstra, F. G. Kondev, M. McCormick, X. Xu, and B. Pfeiffer, *Chin. Phys. C* **36**, 1287 (2012).
- [17] Z. H. Li and H.-J. Schulze, *Phys. Rev. C* **78**, 028801 (2008).
- [18] A. Akmal, V. R. Pandharipande, and D. G. Ravenhall, *Phys. Rev. C* **58**, 1804 (1998).
- [19] S. Gandolfi, J. Carlson, and S. Reddy, *Phys. Rev. C* **85**, 032801(R) (2012).
- [20] N. Chamel, A. F. Fantina, J. M. Pearson, and S. Goriely, *Phys. Rev. C* **84**, 062802 (2011).
- [21] N. Chamel, A. F. Fantina, J. M. Pearson, and S. Goriely, *Astron. Astrophys.* **553**, A22 (2013).
- [22] S. Goriely, N. Chamel, and J. M. Pearson, *Phys. Rev. C* **88**, 061302(R) (2013).
- [23] N. Chamel, Z. K. Stoyanov, L. M. Mihailov *et al.*, *Phys. Rev. C* **91**, 065801 (2015).
- [24] A. F. Fantina, N. Chamel, Y. D. Mutafchieva, Zh. K. Stoyanov, L. M. Mihailov, and R. L. Pavlov, *Phys. Rev. C* **93**, 015801 (2016).
- [25] S. Goriely and G. Martinez-Pinedo, *Nucl. Phys. A* **944**, 158 (2015).
- [26] S. Goriely, *Nucl. Phys. A* **933**, 68 (2015).
- [27] S. Goriely, N. Chamel, and J. M. Pearson, *Phys. Rev. Lett.* **102**, 152503 (2009).
- [28] N. Chamel, S. Goriely, and J. M. Pearson, *Nucl. Phys. A* **812**, 72 (2008).
- [29] S. Goriely, N. Chamel, and J. M. Pearson, *Eur. Phys. J. A* **42**, 547 (2009).
- [30] L. G. Cao, U. Lombardo, and P. Schuck, *Phys. Rev. C* **74**, 064301 (2006).
- [31] N. Chamel, *Phys. Rev. C* **82**, 014313 (2010).
- [32] I. Angeli and K. P. Marinova, *At. Data Nucl. Data Tables* **99**, 69 (2013).
- [33] W. Zuo, I. Bombaci, and U. Lombardo, *Phys. Rev. C* **60**, 024605 (1999).
- [34] W. Zuo, A. Lejeune, U. Lombardo, and J.-F. Mathiot, *Nucl. Phys. A* **706**, 418 (2002).
- [35] G. Colò, N. V. Giai, J. Meyer, K. Bennaceur, and P. Bonche, *Phys. Rev. C* **70**, 024307 (2004).
- [36] P. Danielewicz, R. Lacey, and W. G. Lynch, *Science* **298**, 1592 (2002).
- [37] W. G. Lynch *et al.*, *Prog. Part. Nucl. Phys.* **62**, 427 (2009).
- [38] P. Möller and J. R. Nix, *At. Data Nucl. Data Tables* **39**, 213 (1988).
- [39] S. A. Fayans and D. Zawischa, *Phys. Lett. B* **383**, 19 (1996).
- [40] H. Esbensen, G. F. Bertsch, and K. Hencken, *Phys. Rev. C* **56**, 3054 (1997).
- [41] I. Tews, T. Krüger, K. Hebeler, and A. Schwenk, *Phys. Rev. Lett.* **110**, 032504 (2013).
- [42] M. B. Tsang, J. R. Stone, F. Camera *et al.*, *Phys. Rev. C* **86**, 015803 (2012).
- [43] J. M. Lattimer and Y. Lim, *Astrophys. J.* **771**, 51 (2013).
- [44] M. B. Tsang, Y. Zhang, P. Danielewicz, M. Famiano, Z. Li, W. G. Lynch, and A. W. Steiner, *Phys. Rev. Lett.* **102**, 122701 (2009).
- [45] L.-W. Chen, C. M. Ko, B.-A. Li, and J. Xu, *Phys. Rev. C* **82**, 024321 (2010).
- [46] L. Trippa, G. Colò, and E. Vigezzi, *Phys. Rev. C* **77**, 061304(R) (2008).
- [47] J. Jastrzebski, A. Trzcinska, P. Lubinski, B. Klos, F. J. Hartmann, T. von Egidy, and S. Wycech, *Int. J. Mod. Phys. E* **13**, 343 (2004).
- [48] C. Mondal, B. K. Agrawal, and J. N. De, *Phys. Rev. C* **92**, 024302 (2015).
- [49] B. L. Berman and S. C. Fultz, *Rev. Mod. Phys.* **47**, 713 (1975).
- [50] T. Lesinski, K. Bennaceur, T. Duguet, and J. Meyer, *Phys. Rev. C* **74**, 044315 (2006).
- [51] U. Lombardo (private communication); X. R. Zhou, G. F. Burgio, U. Lombardo, H.-J. Schulze, and W. Zuo, *Phys. Rev. C* **69**, 018801 (2004).
- [52] A. B. Volkov, *Nucl. Phys. A* **141**, 337 (1970).
- [53] G. Saunier, B. Rouben, and J. M. Pearson, *Phys. Lett. B* **48**, 293 (1974).
- [54] P. B. Demorest, T. Pennucci, S. M. Ransom, M. S. E. Roberts, and J. W. T. Hessels, *Nature* **467**, 1081 (2010).
- [55] J. Antoniadis *et al.*, *Science* **340**, 1233232 (2013).
- [56] R. C. Tolman, *Phys. Rev.* **55**, 364 (1939).
- [57] J. R. Oppenheimer and G. M. Volkoff, *Phys. Rev.* **55**, 374 (1939).
- [58] J. Y. Zeng, T. H. Jin, and Z. J. Zhao, *Phys. Rev. C* **50**, 1388 (1994).
- [59] S. Goriely, S. Hilaire, M. Girod, and S. Péru, *Phys. Rev. Lett.* **102**, 242501 (2009).